https://doi.org/10.26599/FRICT.2025.9441207

Research Article

Manipulating conversion of nanoscale wear debris into tribofilm for wear reduction of steel

Hujun Wang, Zhengcan Xie, Hongcai Huang, Wei Liu, Jing Zheng*, Zhongrong Zhou*

Tribology Research Institute, State Key Laboratory of Rail Transit Vehicle System, School of Mechanical Engineering, Southwest Jiaotong University, Chengdu 610031, China

*Corresponding author: Jing ZHENG, jzheng168@home.swjtu.edu.cn; Zhongrong ZHOU, zrzhou@swjtu.edu.cn

Received: August 10, 2025; Revised: December 2, 2025; Accepted: December 15, 2025

Abstract: Wear debris particles play a crucial role in frictional interfaces. Conventional understanding holds that the debris accumulation causes severe wear. Interestingly, the debris from metal friction pairs includes anti-wear metal oxides generated by tribochemical reactions, which can form a protective oxidation film to resist wear. However, minimizing the abrasive damage caused by accumulated debris and using the anti-wear property of the metal oxides can be mutually exclusive. Here, a rational design of a coupling surface that manipulates nanoscale wear debris to resist further wear is reported. It consists of surface textures used to capture and temporarily store excess nanoscale wear debris, a deposited self-cleaning coating that subsequently helps transfer part of the captured debris into the sliding-contact interface, where it converts into a protective oxidation film. The coexistence of the two elements with contrasting properties in manipulating nanoscale wear debris considerably reduces wear under conditions of water lubrication, oil lubrication, and macroscale superlubricity. Our strategy achieves the manipulation and utilization of wear debris for anti-wear purposes. This work holds the potential to promote further investigation into the role of nanoscale wear debris and its utilization approaches.

Keywords: nanoscale wear debris, tribofilm, self-cleaning, surface texture

Highlights

Nanoscale wear debris is manipulated to form a tribofilm to resist wear

Surface texture and self-cleaning coating are used to manipulate the debris

It remains effective under aqueous, oily, and superlubric conditions

1. Introduction

Friction is a ubiquitous phenomenon in mechanical moving parts and consumes approximately 30% of the world's primary energy[1-4]. Issues such as wear and temperature rise caused by friction have a significant effect on the operation efficiency and lifespan of mechanical parts. It is estimated that 80% of mechanical part failures are attributed to wear, and the wear-related costs exceed 2500 Billion Euro per year[5-7]. So far, many strategies have emerged to control friction and wear, including material design, surface treatments, and lubricant additives, and so forth[8-22]. However, wear is almost unavoidable when the surfaces of mechanical parts in relative motion come into contact. Once wear occurs, the resulting wear debris particles play a critical role at the frictional interface. The accumulation of the debris is generally considered harmful because it can easily give rise to high frictional instability and severe wear losses[23].

Conventional approaches for reducing the accumulation of the debris rely on the regular cleaning of the debris and installation of separators in lubrication systems[24]. Surface textures have also been developed to capture and store the excess debris[25-27]. Overall, for the already generated debris, people always attempt to weaken its negative effects from the perspective of removing wear debris. Metals are the most used engineering materials, the debris from metal friction pairs includes metal oxides generated by tribochemical reactions, which can form a protective oxidation film to resist wear[7,28-33]. If the debris can be well manipulated to convert into protective tribofilm for better resisting further wear, it may no longer be considered waste but rather a resource capable of prolonging the service life of mechanical parts. However, minimizing the abrasive effect of the debris and using the anti-wear property of the metal oxides in the debris can be mutually exclusive. How to manipulate the conversion of the debris into protective tribofilm to better resist wear remains a mystery and a

challenge nowadays.

Here, we proposed to construct a bioinspired coupling surface (BCS) with key elements having contrasting properties in manipulating nanoscale wear debris (Fig. 1A,B). The serrated textures of the BCS were elaborately designed with two considerations. (i) They can effectively capture and temporarily store excess wear debris. (ii) The spacing of the textures is sufficiently large to prevent any potential influence of hydrodynamic pressure on the wear-resistance behavior of wear debris. Considering the excellent self-cleaning property of wetting-resistant surfaces[34-37], a superomniphobic coating was applied in the textures to facilitate the transfer of some captured nanoscale wear debris into the sliding-contact interface, allowing it to deposit on the worn surface and form a protective tribofilm for resisting further wear. The seamless integration of the two elements considerably reduced wear under conditions of water lubrication, oil lubrication, and macroscale superlubricity with a coefficient of friction (COF) of less than 0.01, without sacrificing the COF.

2. Materials and Methods

2.1 Materials

AISI 440C steel plates with a hardness of 59 HRC and AISI 440C steel balls (diameter = 10 mm) with a hardness of 60 HRC were obtained from retail stores. The chemical composition of the steel was shown in Table S1. SiO_2 nanoparticles (99.9%) with approximate diameters of 500 nm and 60 nm were purchased from Beijing Deke Daojin Science and Technology Co., Ltd. Trichloro (1H,1H,2H,2H-tridecafluoro-n-octyl) silane (> 97%) and polyethylene glycol (> 99%, MW = 10000) were obtained from Shanghai Aladdin Bio-Chem Technology Co., Ltd. Anhydrous ethanol (AR) and n-hexane (> 95%) were purchased from Chengdu Kelong Chemical Co.,Ltd. Epoxy resin (E51) and polyamide (PA 650) were obtained from Hangzhou Wuhui Port Adhesive Co.,

Ltd. Phytic acid solution (70%) and iron nanoparticles (> 99.9%) with a diameter of approximately 50 nm were purchased from Shanghai Macklin Biochemical Co., Ltd.

2.2 Preparation of liquid-repellent paint

First, 1.34 g of SiO_2 nanoparticles with a diameter of approximately 60 nm were added to 50 mL of n-hexane, followed by ultrasonic treatment for 5 min. Then, 250 μL of trichloro (1H,1H,2H,2H-tridecafluorooctyl) silane was added, and the solution was magnetically stirred at room temperature for 2 h. Fluorinated SiO_2 nanoparticles were obtained by centrifugation, washing, and drying.

SiO_2 nanoparticles (0.196 g) with a diameter of approximately 500 nm were added to 16 mL of anhydrous ethanol. After ultrasonic treatment for 10 min and magnetic stirring for 30 min, E51 (0.033 g) and PA 650 (0.033 g) were added. After stirring the solution for 1 h, paint A was obtained. To prepare paint B, 0.17 g of fluorinated SiO_2 nanoparticles were added to 4 mL of anhydrous ethanol, followed by 10 min of ultrasonic treatment and 30 min of magnetic stirring.

2.3 Preparation of BCS

The designed textures were prepared on the polished 440C steel (R_a = 0.06 μm) by femtosecond laser with a power of 1.5 W, a repetition rate of 100 kHz, and a scanning speed of 300 mm/s. Then, the paint A was coated onto the textured surfaces, and the excess paint was scraped off. After the volatilization of the solvent, the paint B was coated onto the surfaces. The excess paint was also scraped off, and then the residual coating in the non-textured regions was further removed using a filter paper. Finally, the samples were placed in an oven at 60 ºC for 12 h to obtain the BCS.

2.4 Friction tests

Before the tests, the steel balls were cleaned in anhydrous ethanol. Reciprocating ball-on-disc tribological experiments with a sliding stroke of 4 mm were performed on a

UMT tribometer (UMT-TriboLab, Bruker) for 15 min each time. Under water lubrication, the applied load and frequency were 1 N and 12 Hz, respectively. At the beginning of the tests, 20 μL of deionized water was supplied onto the sample surfaces. Under oil lubrication, the applied load was increased to 40 N, and 5 μL of PAO10 was added to perform the tests with a frequency of 12 Hz. To achieve macroscale superlubricity, 20 μL of lubricant consisting of 35 wt% polyethylene glycol, 65 wt% deionized water, 0.1 wt% phytic acid solution, and 0.01 wt% graphene oxide was prepared for the tests, which were conducted under a load of 10 N and at a frequency of 12 Hz. All friction tests for each sample and condition were performed at least three times. The average wear rate and COF were expressed as the mean ± standard deviation.

2.5 Numerical simulations

The motion behavior of nanoscale wear debris in the textures of the sample B and BSC was analyzed using COMSOL Multiphysics software. The width and depth of the texture were 120 μm and 15 μm, respectively, with a channel gap of 100 nm. The iron nanoparticles possessed a diameter of 65 nm. The flow velocity of inlet fluid was set to 96 mm/s. For the BCS, the boundary slip length on the solid surface within the texture was set to 4 μm. The particle tracking was carried out based on Newton's second law of motion. The particles were released through a grid from the wall surface near the fluid inlet, and gravity and drag forces were applied.

2.6 Other characterizations

The contact angles (CAs) and sliding angles (SAs) of 8 μL of water and PAO10 were examined by an optical contact angle meter (SDC-200S, Sindin). The average value was calculated after at least six tests.

Surface morphologies were characterized by scanning electron microscope (SEM, Gemini 300, Zeiss and Apreo 2C, Thermo Fisher Scientific) and laser scanning confocal

microscopy (LSCM, VK-X1000, Keyence). The surface chemical compositions were examined by X-ray photoelectron spectroscopy (XPS, K-Alpha, Thermo Fisher Scientific), time of flight secondary ion mass spectrometry (TOF-SIMS, PHI nanoTOF II, ULVAC-PHI), and energy dispersive spectrometer (EDS, Xplore 30, Oxford).

3. Results and Discussion

The fabrication of the BCS started by sculpting serrated textures (width $W \approx 60$ μm, angle $\alpha \approx 60°$, depth $D \approx 15$ μm, spacing $S \approx 1200$ μm) through femtosecond laser (Fig. S1). Then a superomniphobic coating was deposited in the textures (Fig. 1C), having no obvious effect on the geometric parameters of the textures (Fig. S2). After coating, the Si content in the smooth region of the textured surface was almost negligible compared to that within the texture, indicating that the coating was deposited in the textures rather than other regions (Fig. S3). The coating was designed with an adhesive layer composed of epoxy resin and larger SiO_2 nanoparticles (diameter ≈500 nm, Fig. S4A,B) as the bottom layer, and a top layer of fluorinated smaller SiO_2 nanoparticles (diameter ≈ 60 nm, Fig. S4 C,D,E). To better examine the structure and superomniphobicity of the coating, we deposited it on a glass slide. It exhibited a bilayer structure and a repellence to lubricants of water and poly-α-olefin (PAO10) (Fig. S5). Despite of the deposition of the superomniphobic coating into the textures, it did not affect the apparent wettability of the textured surfaces (Fig. S6). We also built two control samples, one without texture and coating (A), and the other with textures but no coating (B).

Fig. 2A-D demonstrates the strong contrasts observed after reciprocating ball-on-plate tribological tests under water lubrication (Fig. S7A). We evaluated the wear rate by $k = V/(FL)$, where V was the wear volume, F was the applied load, and L was the sliding distance. Notably, the wear rate of the center position between two rows of

textures was calculated for all the textured surfaces. The sample A showed numerous parallel furrows in the wear scar, indicating obvious abrasive wear (wear rate = 4.46 × 10^{-6} mm^3/Nm). For the sample B, clear furrows and a high wear rate (4.54 × 10^{-6} mm^3/Nm) were also observed. In a sharp contrast, only very slight scratches were present on the BCS, and the corresponding wear rate (2.08 × 10^{-6} mm^3/Nm) was much lower than that of the samples A and B. Moreover, high-magnification SEM images revealed no scratches on the BCS surface, while prominent scratches were observed on the samples A and B. This suggests that there was a mechanism capable of reducing the plowing of the microscopic rough peaks on the ball against the BCS. It was noteworthy that, compared to the sample A, the construction of the BCS did not result in an increase in the COF (Fig. S7B).

To date, various mechanisms of friction reduction and wear resistance through surface textures have been proposed, mainly involving the enhancement of hydrodynamic pressure, storage of lubricants to provide secondary lubrication, capture of wear debris, and reduction of contact stress[38-45]. Among them, improving hydrodynamic pressure has received widespread attention. To avoid the situation where the hypothesis of wear debris resisting wear cannot be verified due to the difficult-to-decouple mechanisms, our comparative tribological experiments were carefully designed. The spacing of the designed textures was sufficiently large, ensuring that the width of the wear scars was much smaller than the texture spacing (Fig. 2C). Consequently, it was inferred that when the counter ball moved to the center position between two rows of textures, the textures would not reduce wear by improving hydrodynamic pressure. The geometric parameters of the textures of the sample B and BCS were similar to ensure consistent storage capacity of wear debris and uniform distribution of contact stress. Furthermore, conducting tribological tests under

conditions of sufficient lubricant supply significantly decreased the influence of secondary lubrication effects.

The existing anti-wear mechanisms of surface textures were clearly insufficient to explain the wear resistance observed in the BCS. How did the integration of the BCS with opposite property in manipulating wear debris resist wear? We first resorted to an XPS analysis which was performed in the worn regions (Fig. 2E,F). The deconvolution of the Fe 2p peak revealed the presence of Fe, Fe^{2+} (FeO), Fe^{3+} (Fe_2O_3/FeOOH), respectively[46-48]. Obviously, oxidative wear occurred during rubbing. O 1s peak was deconvoluted into four peaks, which corresponded to C-O (533.0 eV), C=O (532.1 eV), OH^-(531.2 eV) and O^{2-}(530.2 eV)[49,50]. The relative content of FeOOH to Fe_2O_3 was estimated from the OH^- peaks. For the samples A and B, the worn regions exhibited similar relative contents of Fe^{3+} and OH^-, meaning the similar relative content of FeOOH which was generated through tribochemical reactions (Table S2, S3). By contrast, the relative content of FeOOH in the worn region of the BCS was higher than that of the samples A and B, corresponding to their respective wear behaviors.

In addition to the main component Fe, 440C steel also contains small amounts of other metal elements with Cr being the most abundant. From the XPS spectra of Cr 2p, it was seen that the relative content of $Cr(OH)_3$ on the worn region of the BCS was about 23.6% higher than that of the samples A and B, confirming that more metal hydroxides were generated in the worn region of the BCS (Fig. S8). Of course, the SiO_2 nanoparticles in the superomniphobic coating may enter the friction interface and potentially form $Si(OH)_4$ in the presence of water. However, the XPS survey spectra showed a extremely low Si content (Fig. S9). Even if $Si(OH)_4$ was generated, it would have negligible effect on the estimation of the relative content of FeOOH to Fe_2O_3. Considering the low wear rate of the BCS, the relatively higher content of FeOOH was

unlikely to result from more severe oxidative wear. It was most likely due to that more oxidative wear-related debris was deposited in the worn region with the help of the superomniphobic coating. Because of the presence of water, part of the iron oxides in the deposited debris would transform into FeOOH by tribochemical reactions (eqs 1 and 2).

$$Fe_2O_3 + H_2O \rightarrow 2FeOOH \quad (1)$$

$$2FeO + 1/2O_2 + H_2O \rightarrow 2FeOOH \quad (2)$$

We then discussed the evolution of wear debris. Fig. 3A,B shows that the wear debris on both sides of the wear scar of the sample B was more abundant than that of the sample A. Considering the similar wear rate of the samples A and B, it was inferred that the serrated textures of the sample B effectively captured the debris, which was confirmed by the nanoscale debris shown in Fig. 3C. For the BCS, nanoscale wear debris was also captured by the textures (Fig. 3D). We examined the self-cleaning performance of the deposited superomniphobic coating. Both water and PAO10 were capable of effectively cleaning the debris mimicked by iron powder from the coated surface (Fig. 3E). Combined with the XPS analysis results, it was reasonably speculated that part of the debris stored in the textures of the BCS would be brought into the sliding-contact interface. The iron oxides in the debris generated more FeOOH through tribochemical reactions. This was confirmed by more related ionic fragments ($FeO_2H_2^-$, $Fe_2O_2H^-$ and $Fe_2O_3H^-$) in the worn region of the BCS when compared to the sample A, as observed in the TOF-SIMS spectra (Fig. 3F,G). To further demonstrate that the self-cleaning coating facilitated the re-entry of the nanoscale debris into the sliding-contact interface and its deposition on the worn surface, we added iron nanoparticles with a diameter of 50 nm into water to mimic the debris (Fig. S10). As shown in Fig. 3H, the wear rate of the sample B was slightly lower than that of the sample A, while the wear

rate of the BCS was significantly lower than that of the both samples. From the XPS spectra in Fig. 3I,J, it was found that the content of FeOOH in the worn region of the BCS was higher than that of the samples A and B (Table S4, S5). The relative content of $Cr(OH)_3$ also showed the same trend (Fig. S11) These results confirmed that part of the oxidative wear-related debris could be brought into the sliding-contact interface, forming a protective oxidation film to resist further wear.

Although the above analysis can successfully explain the wear resistance of the BCS, other potential anti-wear mechanisms should be further revealed. During the friction process, the epoxy resin and silica nanoparticles that constituted the self-cleaning coating might peel off to act as lubricants. Therefore, the coating was deposited on the sample A. As shown in Fig. S12, the wear rate of the coated sample A was higher than that of the uncoated sample A, indicating that the possibly peeled coating did not contribute to the wear resistance of the BCS. Fig. 3D shows the presence of nanoscale rod-shaped wear debris in the texture of the BCS. Could the rod-shaped debris contribute to wear resistance by acting as rolling bearings? We performed tribological tests under oil lubrication. The wear rate of the sample A, sample B, and BCS was 8.16×10^{-9} mm^3/Nm, 9.55×10^{-9} mm^3/Nm and 4.09×10^{-9} mm^3/Nm, respectively, demonstrating the wear resistance of the BCS under oil lubrication (Fig. 3K). Fig. S13 shows that no rod-shaped wear debris was present in the texture of the BCS. Therefore, we inferred that the contribution of the rolling bearing effect of the rod-shaped debris to the wear resistance of the BCS was very limited under water lubrication. Notably, under surface contact and oil lubrication conditions, surface textures can improve tribological performance by mechanisms such as storing lubricants and modifying hydrodynamic behaviors[51,52]. However, in our friction tests, the contact configuration was a point contact, the texture spacing was as large as 1 mm,

and 5 μL of oil was sufficient to fully cover the 4 mm-long friction path. Consequently, the conventional anti-wear mechanism of surface textures, which operated by influencing oil film thickness, oil distribution, and oil film pressure, was not the primary reason for the anti-wear property of the BCS. It was confirmed that the wear resistance of the BCS resulted from the re-entry of wear debris into the sliding-contact interface, where the debris subsequently deposited. Moreover, BCS could manipulate wear debris to resist wear under both water and oil lubrication, demonstrating the broad applicability of its anti-wear mechanism.

Controlling the geometric parameters of the textures of the BCS was also important for manipulating wear debris to resist wear, as it affected the generation, capture, and transfer of the debris (Fig. S14). The textured area density was defined as $r = W/[S\times\sin(\alpha/2)]$. When α was varied between 30° and 180° ($r \approx 10\%$, $W \approx 60$ μm, $D \approx 15$ μm) through changing the processing parameters of femtosecond laser, we observed that both sharp and dull serrated textures were not appropriate for the design of an efficient BCS. This was most likely due to the dull serrated textures tending to direct the debris away from the worn region in a direction perpendicular to the sliding direction, making it difficult for the debris to re-enter the sliding-contact interface. Overly sharp textures caused increased contact stress, leading to greater wear in the textured region and thus generating excessive debris. The debris might be then brought into the sliding-contact interface, which compromised the integrity of the lubricating film. The optimum in wear rate was observed around $\alpha = 60°$. When S was varied between 960 μm and 2400 μm ($\alpha \approx 60°$, $W \approx 60$ μm, $D \approx 15$ μm), the BCS with S of 1200 μm showed the lowest wear rate. This was most likely due to the fact that textures with high S were difficult to capture adequate debris. By contrast, textures with small S captured excessive debris that might re-enter the sliding-contact interface,

compromising the integrity of the lubricating film. D should also be carefully designed to better manipulate the debris. At small D (5 μm and 10 μm), the debris stored in the texture was most likely to be compacted by the counter ball, which increased the difficulty of transferring the debris to the sliding-contact interface. At high D (20 μm), the transfer of the debris also became more difficult. The optimal D was observed at around 15 μm ($r \approx 10\%$, $\alpha \approx 60°$, $W \approx 60$ μm). Taking into account the effect of W, the optimal W was approximately 60 μm ($r \approx 10\%$, $\alpha \approx 60°$, $D \approx 15$ μm). A high W (75 μm) resulted in a larger portion of the counter ball trapped in the textures. As W decreased from 60 μm to 30 μm, the number of the textures increased due to the constant texture density, leading to more frequent contact between the counter ball and the texture edges. In both cases, wear was exacerbated, leading to the generation of excessive debris.

Taken together, the anti-wear mechanism of the BCS was described in three stages (Fig. 4A). At stage I, the textures of the BCS captured moderate nanoscale wear debris. Subsequently, some debris stored in the textures was brought into the sliding-contact interface (stage II). Finally, part of debris was deposited to repair the furrows, forming a protective oxidation film to resist further wear (stage III). To confirm the self-cleaning behavior of the debris, numerical simulation was performed as shown in Fig. S15 and described in section 2.5. Fig. 4B shows that most of the captured wear debris particles were transferred out of the textures deposited with a self-cleaning coating within 20.3 ms. In contrast, most wear debris particles remained in the textures without the self-cleaning coating (Fig. S16). Obviously, the coating demonstrated good self-cleaning properties. Notably, the nanoscale nature of wear debris played a critical role in manipulating the debris to resist wear. This was because moderate accumulations of the nanoscale debris did not exacerbate wear, as evidenced by the similar wear rates observed in the samples A and B. In this situation, BCS better used the anti-wear

property of the iron oxides in the debris.

Finally, we attempted to decrease the number of textures to reduce the time and energy consumption during texture preparations. The resulting samples, one with the self-cleaning coating and the other without, were designated as B1 and BCS1, respectively (Fig. 5A). That is to say, the optimized samples B and BCS were referred to as B1 and BCS1, respectively. Under water lubrication, BCS1 demonstrated a significantly reduced wear rate (2.21×10^{-6} mm^3/Nm) compared to the sample A, while the sample B1 showed a high wear rate (4.52×10^{-6} mm^3/Nm) (Fig. 5B). Under oil lubrication, BCS1 exhibited good wear resistance (wear rate = 3.98×10^{-9} mm^3/Nm), whereas the wear rate of the sample B1 was similar to that of the sample A (Fig. 5C). In both cases, BCS1 did not increase the COF (Fig. 5D). Interestingly, when the lubricant was a mixture of water, polyethylene glycol, phytic acid and graphene oxide, BCS1 not only reduced the wear rate by 46.3% but also maintained its macroscale superlubricity (Fig. 5E, F). These results indicated that our design strategy was generic, allowing BCS to manipulate nanoscale wear debris to resist wear under lubrication of various liquids.

4. Conclusion

In summary, we have demonstrated that the BCS with contrasting properties in manipulating nanoscale wear debris enables more iron oxides in the oxidative wear-related debris to deposit onto the sliding-contact interface, thereby forming a protective tribofilm and protecting sliding surfaces against further wear. The textures of the BCS can capture and temporarily store the excess debris, while the self-cleaning coating in the textures facilitates the re-entry of part of the stored debris into the sliding-contact interface. Our design strategy enables a reduction in the wear rate of steel by 50.4%, 51.2%, and 46.3% under conditions of water lubrication, oil lubrication, and macroscale

superlubricity, respectively. Wear debris may no longer be seen as waste, but rather as treasure that can be manipulated to resist wear and extend the service life of mechanical parts. Given that the generation of wear debris is a common phenomenon in mechanical tribopairs, this work may inspire the development of new anti-wear design strategies with wide applications.

Acknowledgment

This work was supported by National Natural Science Foundation of China (No. 52575236 and No. 52105212) and China Postdoctoral Science Foundation (No. 2025T180376).

Declaration of competing interest

The authors have no competing interests to declare that are relevant to the content of this article.

References

[1] K. Holmberg & A. Erdemir. Influence of tribology on global energy consumption, costs and emissions. *Friction* **5**, 263-284 (2017).

[2] P. Wang, H. Liang, L. Jiang & L. M. Qian. Effect of nanoscale surface roughness on sliding friction and wear in mixed lubrication. *Wear* **530**, 204995 (2023).

[3] W. H. Chen. et al. Investigation on anti-wear and corrosion-resistance behavior of steel-steel friction pair enhanced by ionic liquid additives under conductive conditions. *Tribol. Int.* **177**, 108002 (2023).

[4] W. W. Ma. et al. $Ti_3C_2T_X$ MXenes modified with dodecylphosphonic acid as an effective lubricant additive. *Tribol. Int.* **186**, 108565 (2023).

[5] J. B. Luo, M. Liu & L. R. Ma. Origin of friction and the new frictionless technology-Superlubricity: Advancements and future outlook. *Nano Energy* **86**, 106092 (2021).

[6] Y. Z. Li, K. Gao, Y. Zhang, J. G. Jiao, L. Zhang & G. X. Xie. Partially oxidized violet phosphorus as an excellent lubricant additive for tribological applications. *Nano Lett.* **23**, 6292-6300 (2023).

[7] C. Liu. et al. Reactive wear protection through strong and deformable oxide nanocomposite surfaces. *Nat. Commun.* **12**, 5518 (2021).

[8] X. Y. Li, L. Lu, J. G. Li, X. A. Zhang & H. J. Guo. Mechanical properties and deformation mechanisms of gradient nanostructured metals and alloys. *Nat. Rev. Mater.* **5**, 706-723 (2020).

[9] W. Z. Zhai. et al. Recent progress on wear-resistant materials: designs, properties, and applications. *Adv. Sci.* **8**, 2003739 (2021).

[10] D. Kumar. Recent advances in tribology of high entropy alloys: A critical review. *Prog. Mater. Sci.* **136**, 101106 (2023).

[11] Y. Ren. et al. Friction-induced rapid amorphization in a wear-resistant $(CoCrNi)_{88}Mo_{12}$ dual-phase medium-entropy alloy at cryogenic temperature. *Compos. Pt. B-Eng.* **263**, 110833 (2023).

[12] M. M. Rong. et al. High lubricity meets load capacity: cartilage mimicking bilayer structure by brushing up stiff hydrogels from subsurface. *Adv. Funct. Mater.* **30**, 2004062 (2020).

[13] G. Schnell, T. Müller . et al. H. Seitz. Tribological effects of different scaled chevron-shaped microstructures on the Stribeck curve of parallel contacts under unidirectional friction. *Tribol. Int.* **178**, 108099 (2023).

[14] Z. Y. Zhou, Q. Y. Zheng, Y. Li, C. Ding, G. J. Peng & Z. Y. Piao. Research on the mechanism of the two-dimensional ultrasonic surface burnishing process to enhance the wear resistance for aluminum alloy. *Friction* **12**, 490-509 (2024).

[15] D. S. Qian, L. Y. Wu, F. Wang, S. Deng, F. Yin & S. F. Jiang. Tailored carburization gradient microstructure and enhanced wear properties of M50NiL steel via introduced prior cold rolling. *Wear* **540**, 205265 (2024).

[16] C. H. Du. et al. Macro-Superlubricity Induced by Tribocatalysis of High-Entropy Ceramics. *Adv. Mater.* **37**, 2413781 (2025).

[17] Y. M. Song, D. Mandelli, O. Hod, M. Urbakh, M. Ma & Q. S. Zheng. Robust microscale superlubricity in graphite/hexagonal boron nitride layered heterojunctions. *Nat. Mater.* **17**, 894-899 (2018).

[18] X. Y. Ren. et al. Superlubricity under ultrahigh contact pressure enabled by partially oxidized black phosphorus nanosheets. *npj 2D Mater. Appl.* **5**, 44 (2021).

[19] W. Wijanarko, H. Khanmohammadi & N. Espallargas. Ionic liquids as boundary additives in water-based and PAO lubricants. *Friction* **10**, 1405-1423 (2022).

[20] A. Aymard, E. Delplanque, D. Dalmas & J. Scheibert. Designing metainterfaces with specified friction laws. *Science* **383**, 200-204 (2024).

[21] Y. Liu. et al. Bionic jaw-like micro one-way valve for rapid and long-distance water droplet unidirectional spreading. *Nano Lett.* **23**, 5696-5704 (2023).

[22] S. L. Feng. et al. Three-dimensional capillary ratchet-induced liquid directional steering. *Science* **373**, 1344-1348 (2021).

[23] A. Erdemir. et al. Carbon-based tribofilms from lubricating oils. *Nature* **536**, 67-71 (2016).

[24] C. D. Qin, S. Z. He, X. C. Zhou, Q. Q. Li & Z. H. Yang. Research on the effect of nano/micron SiO_2 particles on actual wear of the main gear box of large-scale mechanical equipment. *Tribol. Lett.* **72**, 12 (2024).

[25] N. Zhang, X. H. Zhan, Z. T. Li, Y. C. Liu, J. Ma & J. D. Guo. Effect of squamous textured SiC on the dry-sliding tribological properties of graphite asperities. *Wear* **544**, 205297 (2024).

[26] C. W. Miao, Z. W. Guo & C. Q. Yuan. Tribological behavior of co-textured cylinder liner-piston ring during running-in. *Friction* **10**, 878-890 (2022).

[27] P. D. Srivyas. et al. Synergetic effect of surface texturing and graphene nanoplatelets on the tribological properties of hybrid self-lubricating composite. *Tribol. Int.* **168**, 107434 (2022).

[28] Y. X. Niu, X. J. Pang, S. W. Yue, B. Shanggaun & Y. Z. Zhang. The friction and wear behavior of laser textured surfaces in non-conformal contact under starved lubrication. *Wear* **476**, 203723 (2021).

[29] J. Ma, Y. C. Liu & W. J. Zhang. Synergistic effect of surface sinusoidal textures and oxide layer on tribological properties of 40Cr alloy steel. *Surf. Coat. Technol.* **450**, 128992 (2022).

[30] C. X. Zhang. et al. Wear mechanism of flexspline materials regulated by novel amorphous/crystalline oxide form evolution at frictional interface. *Tribol. Int.* **135**, 335-343 (2019).

[31] Y. Yin. et al. Excellent tribological performance of oil-impregnated porous polyimide rubbing against Cr-rich steel balls. *Tribol. Int.* **190**, 109053 (2023).

[32] K. J. Jin, Z. H. Qiao, S. Y. Zhu, J. Cheng, B. Yin & J. Yang. Tribological properties of bronze–Cr–Ag alloy in seawater, NaCl solution and deionized water. *Tribol. Int.* **98**, 1-9 (2016).

[33] Y. X. Ou, X. P. Ouyang, B. Liao, X. Zhang & S. Zhang. Hard yet tough CrN/Si_3N_4 multilayer coatings deposited by the combined deep oscillation magnetron sputtering and pulsed dc magnetron sputtering. *Appl. Surf. Sci.* **502**, 144168 (2020).

[34] Y. Lu, S. Sathasivam, J. L. Song, C. R. Crick, C. J. Carmalt & I. P. Parkin. Robust self-cleaning surfaces that function when exposed to either air or oil. *Science* **347**, 1132-1135 (2015).

[35] D. H. Wang. et al. Design of robust superhydrophobic surfaces. *Nature* **582**, 55-59 (2020).

[36] W. C. Gu. et al. Ultra-durable superhydrophobic cellular coatings. *Nat. Commun.* **14**, 5953 (2023).

[37] M. M. Liu, J. Li, Y. Y. Hou & Z. G. Guo. Inorganic adhesives for robust superwetting surfaces. *ACS Nano* **11**, 1113-1119 (2017).

[38] Z. Q. Wang, R. H. Ye & J. B. Xiang. The performance of textured surface in friction reducing: A review. *Tribol. Int.* **177**, 108010 (2023).

[39] B. Mao, A. Siddaiah, Y. L. Liao & P. L. Menezes. Laser surface texturing and related techniques for enhancing tribological performance of engineering materials: A review. *J. Manuf. Process* **53**, 153-173 (2020).

[40] P. Lu & R. J. K. Wood. Tribological performance of surface texturing in mechanical applications-A review. S*urf. Topogr. Metrol. Prop.* **8**, 043001 (2020).

[41] W. Wang, W. H. Zhao, P. Z. Guo, Q. Liu, A. N. Kouediatouka & G. N. Dong. A textured surface with oil inflow and outflow function designed for starved lubrication. *Tribol. Int.* **184**, 108450 (2023).

[42] J. Y. Huang, Y. C. Guan & S. Ramakrishna. Tribological behavior of femtosecond laser-textured leaded brass. *Tribol. Int.* **162**, 107115 (2021).

[43] Y. Sun. et al. Experimental evaluation of surface generation and force time-varying characteristics of curvilinear grooved micro end mills fabricated by EDM. *J. Manuf. Process* **73**, 799-814 (2022).

[44] J. Ma, Y. C. Liu, P. Yi, H. Y. Jia, N. Zhang & J. W. Sun. Anti-friction mechanism of sinusoidal texture with various intervals: The synergistic effect of dynamic pressure and tribofilm. *Tribol. Int.* **173**, 107635 (2022).

[45] M. Zimmer, S. C. Vlădescu, L. Mattsson, M. Fowell & T. Reddyhoff. Shear-area variation: A mechanism that reduces hydrodynamic friction in macro-textured piston ring liner contacts. *Tribol. Int.* **161**, 107067 (2021).

[46] I. Uhlig, R. Szargan, H. W. Nesbitt & K. Laajaletho. Surface states and reactivity of pyrite and marcasite. *Appl. Surf. Sci.* **179**, 222-229 (2001).

[47] M. C. Biesinger, B. P. Payne, A. P. Grosvenor, L. W. M. Lau, A. R. Gerson & R. S. C. Smart. Resolving surface chemical states in XPS analysis of first row transition metals, oxides and hydroxides: Cr, Mn, Fe, Co and Ni. *Appl. Surf. Sci.* **257**, 2717-2730 (2011).

[48] T. Yamashita & P. Hayes. Analysis of XPS spectra of Fe^{2+} and Fe^{3+} ions in oxide materials. *Appl. Surf. Sci.* **254**, 2441-2449 (2008).

[49] B. H. Feng. et al. Capillary electroosmosis properties of water lubricants with different electroosmotic additives under a steel-on-steel sliding interface. *Friction* **10**, 1019-1034 (2022)

[50] H. Nohira. et al. Characterization of ALCVD-Al_2O_3 and ZrO_2 layer using X-ray photoelectron spectroscopy. *J. Non-Cryst. Solids* **303**, 83-87 (2002).

[51] A. Janssen, B. Pinedo, A. Igartua, G. Liiskmann, L. Sexton. Study on friction and wear reducing surface micro-structures for a positive displacement pump handling highly abrasive shale oil. *Tribol. Int.* **107**, 1-9 (2017).

[52] Y. Liu, H. Zhang, S.J. Dai, G.N. Dong. Designing a bioinspired scaly textured surface for improving the tribological behaviors of starved lubrication. *Tribol. Int.* **173**, 107594 (2022).

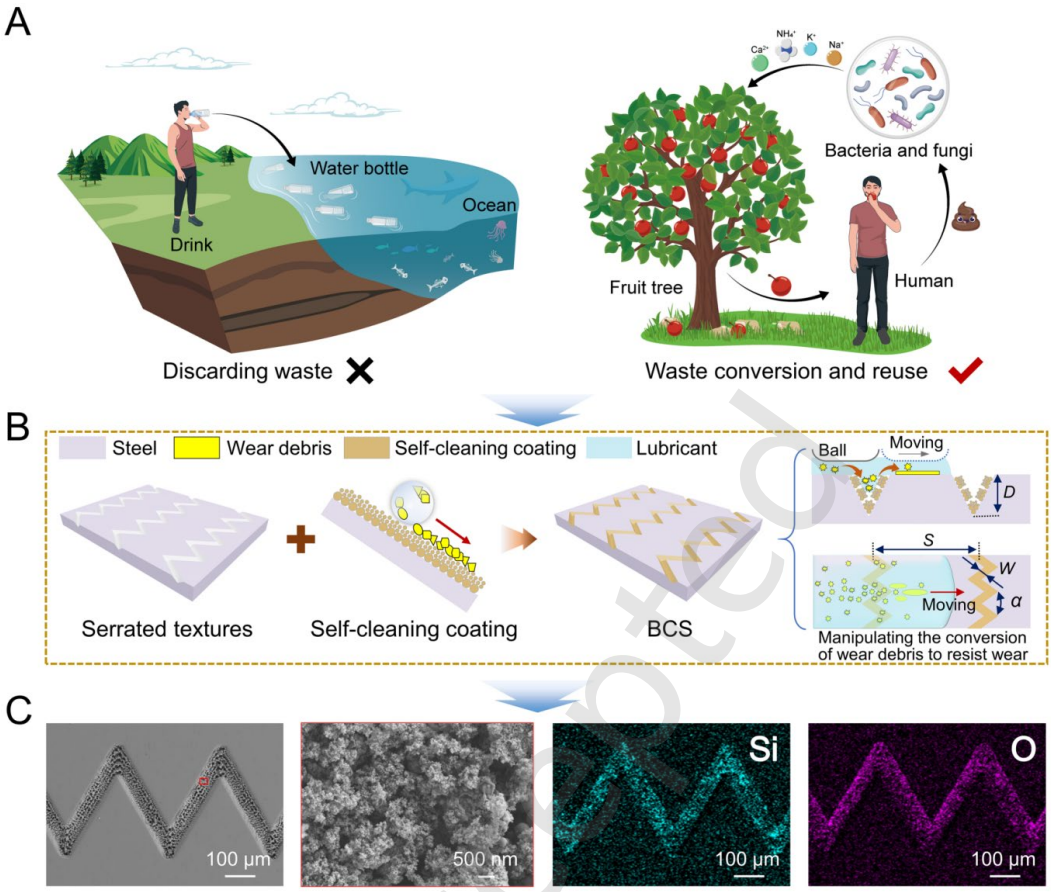

Fig. 1 An overview of our design. (A) A strategy such that the waste should not be directly discarded for the earth sustainable development; it needs to be converted and reused, which provides us with an inspiration to manipulate the conversion of nanoscale wear debris to resist wear. **(B)** Design of the BCS consisting of serrated textures and self-cleaning coatings. The textures can effectively capture and temporarily store wear debris. By contrary, the coatings facilitate the re-entry of some captured debris into the sliding-contact interface, converting into a protective oxidation film to resist further wear. **(C)** SEM images of the BCS and the deposited coating, and EDS mapping images of the BCS.

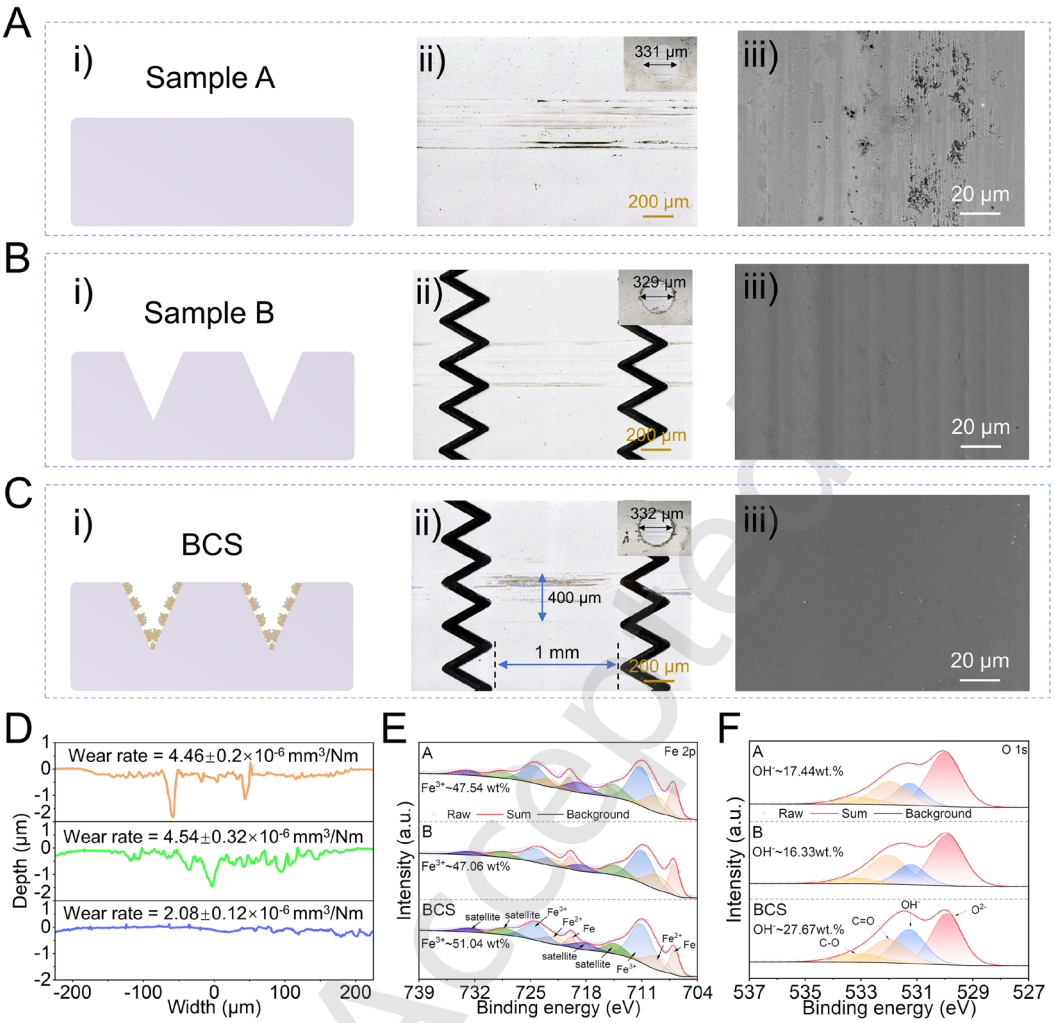

Fig. 2 Comparison in wear behaviors under water lubrication. Characterizations of the worn regions for the **(A)** sample A (no texture and coating), **(B)** sample B (no coating), and **(C)** BCS: (i) schematics of the samples, (ii) LSCM images of the worn samples and counter balls, and (iii) SEM images of the worn samples. **(D)** Profiles corresponding to (ii). XPS spectra of the **(E)** Fe 2p and **(F)** O 1s on the worn regions of the samples.

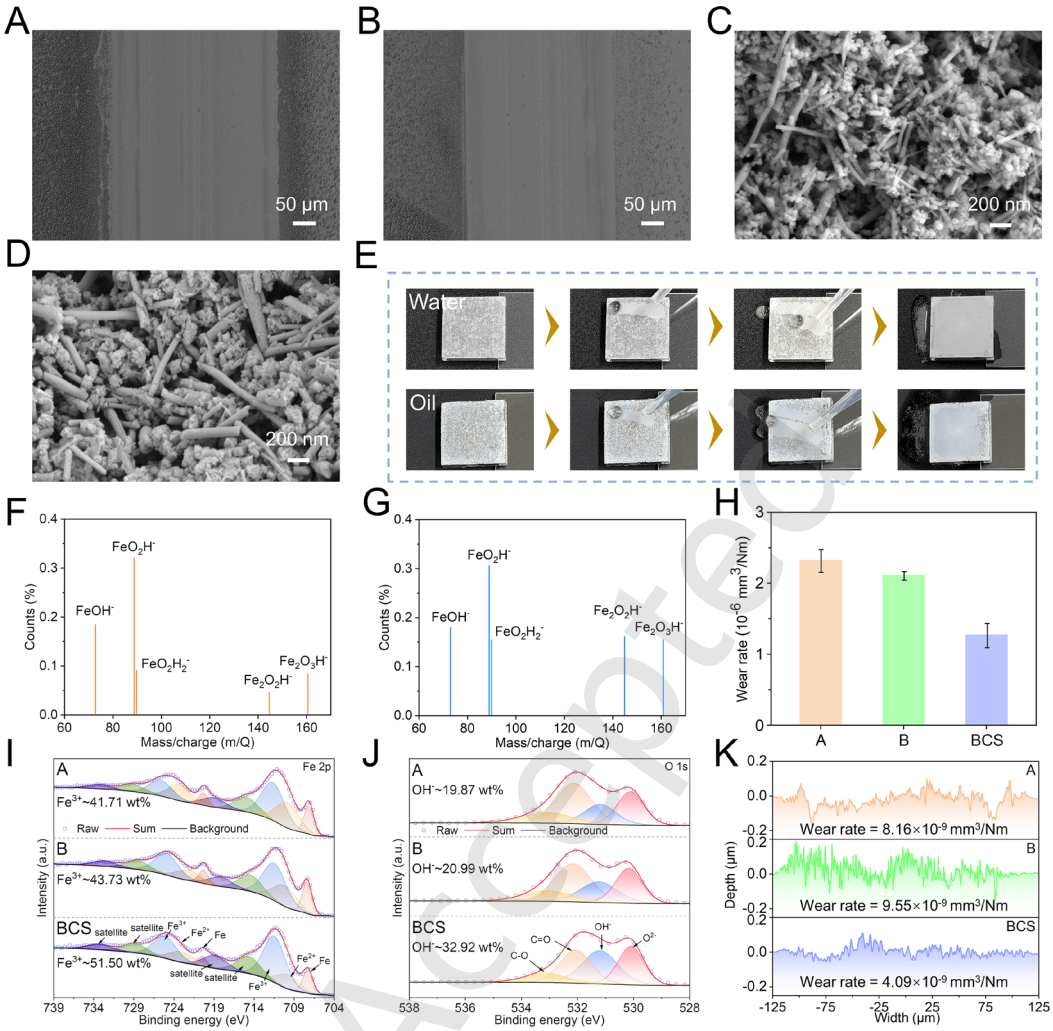

Fig. 3 Analysis of the evolution of wear debris. (A, B) SEM images of the wear debris on both sides of the wear scars of the samples A and B, respectively. **(C, D)** SEM images of the nanoscale wear debris in the textures of the samples B and BCS, respectively. **(E)** Self-cleaning property of the as-prepared coating. **(F, G)** TOF-SIMS spectra of the worn regions of the samples A and BCS, respectively. **(H)** Comparison in wear rate of the three samples lubricated with water containing iron nanoparticles. **(I)** Fe 2p spectra of the sample A, sample B, and BCS lubricated with water containing iron nanoparticles, respectively. **(J)** O 1s spectra corresponding to (I), respectively. **(K)** Profile image of wear scars of the three samples lubricated with oil.

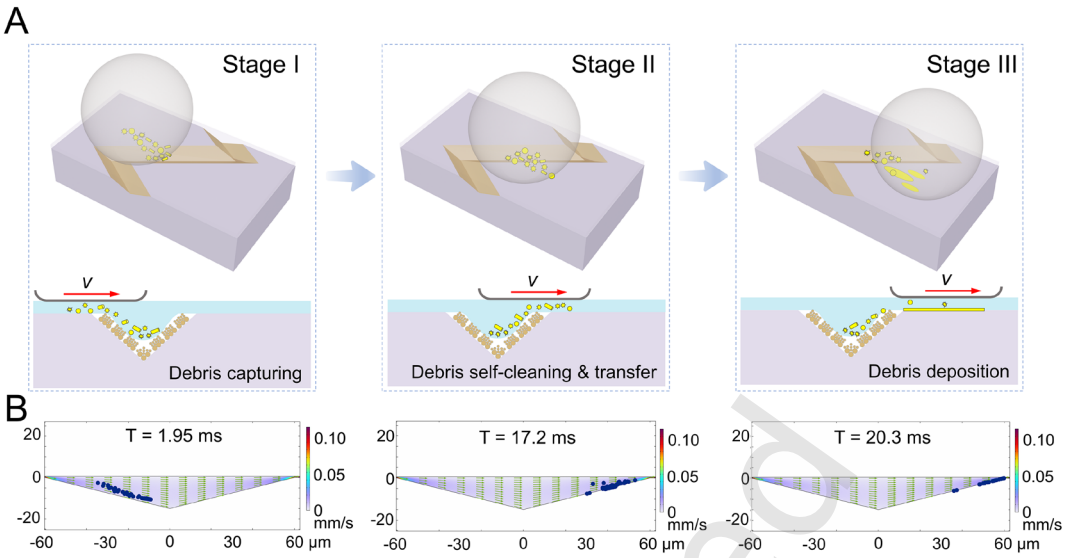

Fig. 4 Analysis of anti-wear mechanism. (A) Some wear debris is captured at stage I; Part of the captured debris re-enters the sliding-contact interface at stage II; At stage III, some iron oxides in the debris are deposited to repair the worn surface, forming a protective oxidation film to resist further wear. **(B)** Numerical simulation of the motion behavior of the nanoscale debris in the texture of the BCS.

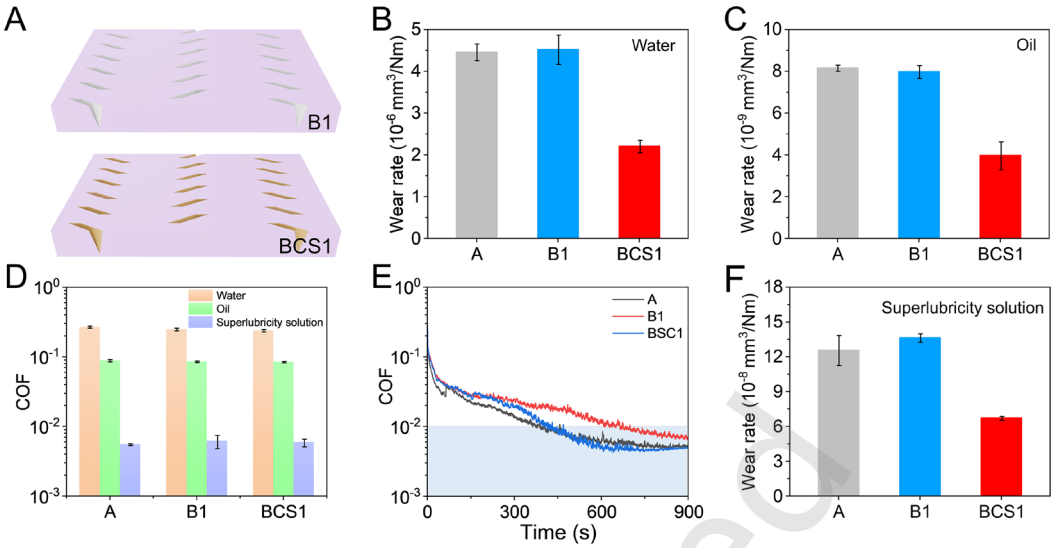

Fig. 5 Performance of the BCS1 with optimized textures. (A) Schematic of the B1 and BCS1 with optimized textures. **(B, C)** Wear rates of the three samples under water and oil lubrication conditions, respectively. **(D)** Comparison of final COFs of the three samples lubricated with different lubricants. Comparisons of **(E)** COF curves and **(F)** Wear rates of the three samples lubricated with a superlubricity solution.

Author biography

Hujun WANG. He received his Ph.D. degree in bionic science and engineering in 2020 from Jilin University, Changchun, China. He joined the Tribology Research Institute at Southwest Jiaotong University in 2020. His current position is an associate professor. His research interest is bionic tribology.

Jing ZHENG. She received her Ph.D. degree in mechanical engineering in 2005 from Southwest Jiaotong University, Chengdu, China. She joined the Tribology Research Institute at Southwest Jiaotong University in 2000. Her current position is a professor. Her research areas cover the tribology of natural teeth and dental materials, bio-lubrication, and bionic tribology.

Zhongrong ZHOU. He received his Ph.D. degree from Ecole Centrale De Lyon, France. After that, he conducted his postdoctoral research at Laval University, Canada. From 1995 to 1997, he was invited to serve as the guest professor in Ecole Centrale De Lyon, France. He has been appointed as the dean of the School of Mechanical Engineering in Southwest Jiaotong University, China, since 2006. His current position is a professor and vice-president of Southwest Jiaotong University. His research interests include tribology, surface engineering technology, and materials science.